On the limits of distinguishing seabed types via ambient acoustic sound \odot

John Lipor (10); John Gebbie (10); Martin Siderius (10)



J. Acoust. Soc. Am. 154, 2892–2903 (2023)

https://doi.org/10.1121/10.0022331













On the limits of distinguishing seabed types via ambient acoustic sound

John Lipor, 1,a) Dohn Gebbie, 2 Dand Martin Siderius 1

ABSTRACT:

This article presents a theoretical analysis of optimally distinguishing among environmental parameters from ocean ambient sound. Recent approaches to this problem either focus on parameter estimation or attempt to classify the environment into one of many known types through machine learning. This classification problem is framed as one of hypothesis testing on the received ambient sound snapshots. The resulting test depends on the Kullback-Leibler divergence (KLD) between the distributions corresponding to different environments or sediment types. Analysis of the KLD shows the dependence on the signal-to-noise ratio, the underlying signal subspace, and the distribution of eigenvalues of the respective covariance matrices. This analysis provides insights into both when and why successful hypothesis testing is possible. Experiments demonstrate that our analysis provides insight as to why certain environmental parameters are more difficult to distinguish than others. Experiments on sediment types from the Naval Oceanographic Office Bottom Sediment type database show that certain types are indistinguishable for a given array configuration. Further, the KLD can be used to provide a quantitative alternative to examining bottom loss curves to predict array processing performance. © 2023 Acoustical Society of America. https://doi.org/10.1121/10.0022331

(Received 26 July 2023; revised 12 October 2023; accepted 18 October 2023; published online 7 November 2023)

[Editor: Peter Gerstoft] Pages: 2892–2903

I. INTRODUCTION

Understanding the composition of the ocean floor is a critical task for the prediction of sonar performance and operation. The seabed type can be parameterized in terms of a geoacoustic model and can have a significant impact on estimation and detection performance of active sonar systems.^{2,3} In recent years, there has been increased interest in estimating environmental parameters passively, utilizing the ambient acoustic sound occurring from surface waves or ships of opportunity. ^{4–8} While many studies focus on highly accurate, offline seabed characterization, 7-12 the ability to determine the seabed type in an online manner can improve the fidelity of sonar performance predictions. Further, refining estimates of the spatial variability of the seabed may involve adaptively guiding autonomous underwater vehicles, which must make decisions based on real-time information. 13,14

Most recently, there has been great interest in applying machine learning techniques to acoustics, ¹⁵ with promising results displayed for both geoacoustic inversion and seabed classification. ^{16–20} However, training such algorithms requires the curation of large datasets, as well as *a priori* knowledge of which seabed types may be encountered. Further, when such approaches fail, it is unclear whether this is due to (1) limits of the machine learning model selected, (2) the training procedure, or (3) fundamental properties of the seabed parameters under consideration.

a)Email: lipor@pdx.edu

Before investing the resources required to generate large datasets for training such algorithms, it is essential to first understand the information-theoretic limits of classification using ambient acoustic sound. Toward this end, we consider a more basic problem: beginning with a reference class whose distribution is perfectly known, our goal is to decide whether snapshots from a given location belong to the reference class or a new class. This task is simpler than a general classification problem and has applications in seabed exploration. In particular, consider the goal of distinguishing between seabed types in the High Frequency Environmental Acoustics (HFEVA) dataset from the Naval Oceanographic Office Bottom Sediment type Database.²¹ In practical settings, the seabed may consist largely of one type (e.g., rock), and the aim is then to discover any locations where the seabed type deviates from this reference. This problem may be framed as a hypothesis test, which is solved by evaluating the likelihood ratio between the two distributions and whose success is governed by the Kullback-Leibler divergence (KLD).

This article introduces a decision-theoretic approach to distinguishing between seabed parameters. Our key contribution is the analysis of the KLD in the case of circularly symmetric complex Gaussians under an additive covariance model. This analysis facilitates a deeper understanding of the fundamental limits of seabed classification, placing the KLD in terms of the signal-to-noise ratio, the underlying subspace structure in the data, and the distribution of the eigenvalues of the respective covariance matrices. We then examine these properties in terms of real seabed parameters

¹Department of Electrical and Computer Engineering, Portland State University, 1900 Southwest 4th Avenue, Suite 160, Portland, Oregon 97201, USA

²Metron, Incorporated, 2020 Southwest 4th Avenue, Suite 170, Portland, Oregon 97201, USA

using data generated by the multidimensional ambient noise model (MDANM),²² which is an ocean ambient sound model and sonar simulator based on the Harrison model,²³ providing insights into when successful hypothesis testing is possible. Finally, we apply our approach to distinguishing between seabed types from the HFEVA database, indicating which seabed types can be reliably distinguished for the given array configuration.

The remainder of this article is organized as follows. Section II describes the decision-theoretic framework for determining whether sets of ambient acoustic snapshots are indicative of distinct seabed types, as well as connections of this framework to the KLD. Section III provides an in-depth analysis of the KLD for the covariance model considered, providing insights into the fundamental limits of hypothesis testing. In Sec. IV, we evaluate the performance of hypothesis testing, analyzing the sensitivity to various environmental parameters of interest, as well as the ability to resolve the various sediment types from the HFEVA database. Finally, Sec. V provides a discussion of these results and additional potential applications.

II. THEORY

This section provides the theoretical limits on distinguishing between geoacoustic properties at two distinct locations using the ambient sound field. Define the N-dimensional vector of geoacoustic parameters of interest to be θ , which is an element of the set of all possible parameters $\Theta \subset \mathbb{R}^N$. Consider an array of M receivers that capture ambient acoustic sound. Each sensor captures a finite-duration time series that is then Fourier transformed, resulting in a snapshot $x \in \mathbb{C}^M$. For a given set of environmental parameters, we assume that the snapshots are drawn from a circularly symmetric complex Gaussian distribution with covariance⁸

$$K_{\theta} = \mathbb{E}[xx^{H}] = \sigma_{s}^{2}\Gamma_{\theta} + \sigma_{n}^{2}I, \tag{1}$$

where σ_s^2 is the power in the ambient sound generated by surface waves, σ_n^2 is the non-acoustic sensor noise variance, and Γ_{θ} is the signal covariance matrix, which is obtained from a model of the ambient sound. Without loss of generality, we assume $\operatorname{tr}(\Gamma_{\theta}) = M$ to match the power in the signal and noise covariances. For such snapshots, the probability density function (PDF) is given as

$$f(x;\theta) = \det(\pi K_{\theta})^{-1} \exp\left(-x^{H} K_{\theta}^{-1} x\right), \tag{2}$$

where det denotes the determinant and the semicolon indicates that θ consists of a vector of non-random model parameters (see the Appendix A, Ref. 38). The above PDF should be viewed as a function of x for a fixed set of environmental parameters θ . This lies in contrast to the setting of maximum likelihood estimation, which is discussed in Sec. II A. We use the notation Γ_0 and Γ_1 to refer to the signal covariances corresponding to parameters θ_0 and θ_1 ,

respectively. We likewise define $K_0 = \sigma_s^2 \Gamma_0 + \sigma_n^2 I$ and $K_1 = \sigma_s^2 \Gamma_1 + \sigma_n^2 I$.

Consider snapshots obtained from two separate physical regions of the seabed. Our goal is to determine whether these snapshots are drawn from the same distribution, which indicates whether they share the same environmental parameters. Classical decision theory indicates this problem can be solved via the generalized likelihood ratio test, ²⁵ detailed in Sec. II A. The goal of this work is to establish fundamental limits on when hypothesis testing can reliably distinguish between two sets of environmental parameters.

A. Hypothesis testing

The statistical approach to distinguishing between two sets of model parameters is known as *hypothesis testing*. The test of whether the seabed parameters are the same at two locations then becomes one of testing the equivalence between the distributions of snapshots at these locations. To establish fundamental limits on distinguishing such parameters, we assume the environment is well studied at a reference location with parameters θ_0 , so that the error in estimating the resulting covariance K_0 is negligible. At each new location, we obtain a set of L snapshots $x_1, ..., x_L$ and wish to test

$$x_1, ..., x_L \sim f(x; \theta_0)$$
 vs $x_1, ..., x_L \sim f(x; \theta_1)$,

where $\theta_1 \neq \theta_0$ is an unknown set of environmental parameters. To formalize this test, we partition the set of possible parameter vectors $\Theta \subset \mathbb{R}^N$ into two subsets Θ_0 and Θ_1 such that $\Theta_0 \cup \Theta_1 = \Theta$ and $\Theta_0 \cap \Theta_1 = \emptyset$. In our setting, $\Theta_0 = \theta_0$ and $\Theta_1 = \Theta \setminus \{\theta_0\}$. The task is to decide between the null hypothesis

$$H_0$$
: $\theta = \theta_0$ (3)

and the alternative hypothesis

$$H_1: \quad \theta \neq \theta_0.$$
 (4)

Let $S \subset \mathbb{C}^M$ be a set of snapshots. To decide between H_0 and H_1 , we define a test statistic $\Lambda(S)$ and critical value or threshold τ such that we decide H_1 when $\Lambda(S) > \tau$ and H_0 otherwise. The threshold τ is a user-defined value that is usually selected to allow a fixed probability of false positives. Formally, define the rejection region as the possible sets of snapshots for which we reject the null hypothesis

$$R = \{ S \subset \mathbb{C}^M : \Lambda(S) > \tau \}. \tag{5}$$

In the case where $\Theta_0 = \theta_0$, the test is said to have *size* or *level* α if $\mathbb{P}_{H_0}(S \in R) \leq \alpha$. In words, the test level is the probability that snapshots drawn under the null hypothesis lie in the rejection region, i.e., the false alarm rate. To obtain a test of level α , the threshold is chosen so that $\mathbb{P}_{H_0}(\Lambda(S) > \tau) = \alpha$.

For the two-sided test above, where the parameters under the alternative hypothesis are unknown, a common

choice of test statistic is the generalized likelihood ratio test (GLRT). Let $\mathcal{L}(\theta)$ be the likelihood of the data under parameters θ .

$$\mathcal{L}(\theta) = \prod_{i=1}^{L} f(x_i; \theta). \tag{6}$$

The GLRT statistic is then defined as

$$\Lambda(x_1, ..., x_L) = 2 \log \frac{\sup_{\theta \in \Theta_1} \mathcal{L}(\theta)}{\sup_{\theta \in \Theta_0} \mathcal{L}(\theta)}.$$
 (7)

The likelihood function is a measure of how well the parameters θ fit the fixed set of observations $x_1, ..., x_L$. In this light, the hypothesis test then becomes one of measuring the most likely parameters under the null hypothesis against those under the alternative hypothesis. In our setting, $\Theta_0 = \theta_0$ is known, and the numerator of Eq. (7) corresponds to the maximum likelihood estimate. This test is asymptotically the uniformly most powerful (UMP), i.e., among all tests with level α , it has (asymptotically) the greatest chance of correctly rejecting samples from the alternative hypothesis. Further, for finite samples, if a UMP test exists, then it corresponds to the GLRT.²⁶

Under the snapshot model defined by Eqs. (1) and (2), the GLRT becomes

$$\Lambda(x_1, ..., x_L) = 2L \left(\log \frac{\det(K_0)}{\det(\hat{K})} - M + \operatorname{tr}\left(K_0^{-1}\hat{K}\right) \right),$$
(8)

where K_0 is the covariance corresponding to the parameters θ_0 , and $\hat{K} = (1/L)\sum_{i=1}^L x_i x_i^H$ is the sample covariance matrix, which is the maximum likelihood estimate of the unknown covariance matrix. Equation (8) is derived in Appendix A.

Figure 1 displays the resulting test statistic and threshold for the "rock" and "gravelly muddy sand" sediment types from the HFEVA dataset. We set the SNR to unity and treat "rock" as the null hypothesis. To select the threshold τ , we utilize the well-known result that the GLRT converges to a χ^2_{ν} distribution with degrees of freedom $\nu = M(M-1)$, which is the number of free variables in the covariance matrix. We choose the threshold to correspond to test level $\alpha = 10^{-4}$. For each region, we generate 50 independent samples of 300 snapshots. Within the "transition" region, we draw a fraction of snapshots from each of the two sediment types, with the proportion from rock decreasing linearly as the plot moves to the right. The figure shows that the test statistic increases rapidly as more snapshots are obtained from the gravelly muddy sand region, and the alternative hypothesis (not rock) is selected for any values of Λ greater than τ .

B. Kullback-Leibler divergence

The KLD²⁷ is a common means of measuring the discrepancy between two distributions and has been utilized in

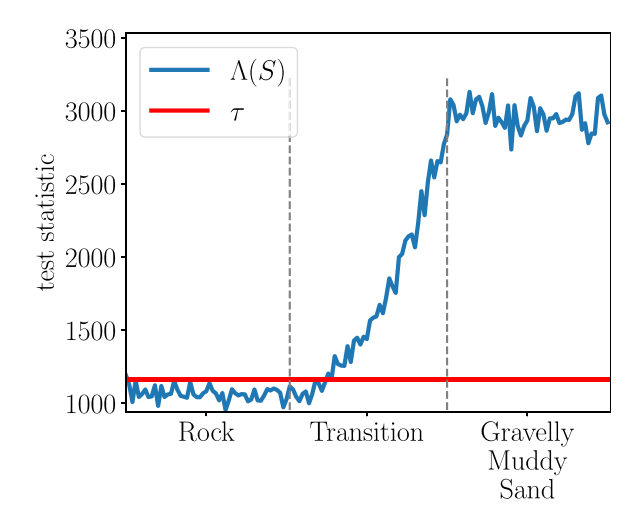


FIG. 1. (Color online) Example hypothesis testing between "Rock" and "Gravelly Muddy Sand" sediment types from HFEVA dataset. In the transition region, the proportion of snapshots from each sediment types varies linearly. The test statistic Λ remains below the threshold τ until the transition region.

acoustic signal classification, 28,29 environmental parameter estimation, 8 and direction of arrival estimation. 30 For two distributions with corresponding parameters θ_0 and θ_1 , the general form of the KLD of the distribution $f(x;\theta_1)$ from $f(x;\theta_0)$ is

$$D(\theta_0||\theta_1) = \int f(x;\theta_0) \log \frac{f(x;\theta_0)}{f(x;\theta_1)} dx.$$
 (9)

The KLD appears frequently in the analysis of various hypothesis tests,³¹ and recent results indicate that high-dimensional hypothesis tests can be shown to approximate the KLD or other divergences.³² From an information-theoretic perspective, the KLD measures the inefficiency in using parameter θ_1 when the true distribution corresponds to θ_0 .³³

In the case of circularly symmetric complex Gaussians, the KLD is shown to be⁸

$$D(\theta_0||\theta_1) = \operatorname{tr}(K_1^{-1}K_0) - M + \log \frac{\det(K_1)}{\det(K_0)}.$$
 (10)

Comparing Eq. (10) to Eq. (8), we see that the GLRT can be placed in terms of the KLD, so that

$$\Lambda(x_1, ..., x_L) = 2LD(\hat{\theta}||\theta_0), \tag{11}$$

where $\hat{\theta}$ refers to the parameters under the maximum likelihood estimate. In light of Eq. (11), we see that the GLRT can be viewed as measuring whether the distribution of snapshots under the null hypothesis is sufficiently far from the distribution under the maximum likelihood estimate.

Interpreting the GLRT in light of the KLD provides a lower bound on which seabed parameters can be distinguished from a set of L snapshots. Consider two sets of parameters θ_0 and θ with true KLD $D(\theta||\theta_0)$. When

estimating this divergence from a set of L snapshots, existing results from parametric estimation of KLD^{34} indicate that the absolute error converges at a rate of $O(1/\sqrt{L})$, i.e.,

$$|D(\theta||\theta_0) - D(\hat{\theta}||\theta_0)| \le \frac{c}{\sqrt{L}},\tag{12}$$

for some c > 0. Equation (12) provides the following lower bound on the estimated KLD:

$$D(\hat{\theta}||\theta_0) \ge D(\theta||\theta_0) - \frac{c}{\sqrt{L}}.$$

Therefore, a sufficient condition to guarantee the estimated KLD is positive is

$$D(\theta||\theta_0) > \frac{c}{\sqrt{L}}. (13)$$

In other words, the estimated KLD may be as small as zero unless the condition (13) is met. Hence, we conclude that no threshold τ can reliably distinguish between the null and alternative hypotheses unless there is a discrepancy of c/\sqrt{L} between the two distributions. Conversely, if the KLD between the estimated and null distributions is greater than c/\sqrt{L} , one may reliably select the alternative hypothesis. We will show in Sec. IV that the threshold chosen to obtain a level of $\alpha=1\times10^{-4}$ corresponds to this bound on the KLD.

III. THEORETICAL CHARACTERIZATION OF KLD

In Sec. II, we showed that the hypothesis testing problem is intrinsically linked to the KLD between the underlying distributions. In this section, we provide a deeper analysis of the KLD between two sets of environmental parameters under the model (1). This allows us to place the KLD in terms of familiar quantities such as the signal-tonoise ratio (SNR) and to disentangle the isotropic sensor noise from the underlying signal covariance matrices. While Sec. II B provides a bound on *when* hypothesis testing can successfully distinguish between seabed parameters, the analysis provided here provides a deeper look as to *why*.

The following theorem quantifies the KLD in terms of the SNR σ_s^2/σ_n^2 and the eigenvalues and eigenvectors of Γ_1 and Γ_2 .

Theorem 1. Consider two zero-mean, circularly symmetric Gaussian distributions characterized by the covariance matrices K_1 and K_0 . Assume these covariances follow the model (1) with parameter vectors θ_1 and θ_0 , respectively. Finally, let $\Gamma_1 = U\Lambda U^H$ and $\Gamma_0 = V\Pi V^H$. Then

$$D(\theta_0||\theta_1) = \text{SNR}\left(M - \sum_{i=1}^{M} \sum_{j=1}^{M} \frac{\pi_i \lambda_j \text{SNR}}{1 + \lambda_j \text{SNR}} |u_j^H v_i|^2\right)$$
$$-\sum_{i=1}^{M} \frac{\lambda_i \text{SNR}}{1 + \lambda_i \text{SNR}} + \sum_{i=1}^{M} \log\left(\frac{\lambda_i \text{SNR} + 1}{\pi_i \text{SNR} + 1}\right). \tag{14}$$

The proof can be found in Appendix B. Theorem 1 allows us to characterize how distinct the two distributions are in terms of the SNR as well as the structure of the signal subspaces defined by Γ_0 and Γ_1 . In what follows, we examine (14) in both the low-rank case and the general case, in order to gain insight into the impact of each term.

A. Low-rank setting

To further understand the divergence as derived in Eq. (14), we consider the case where the signal covariance matrices have rank r and all eigenvalues are equal, having the form $\Gamma_0 = (M/r)VV^H$ and $\Gamma_1 = (M/r)UU^H$, where $U, V \in \mathbb{C}^{M \times r}$ have orthonormal columns spanning the subspace corresponding to each set of parameters. The assumption that there is a signal component lying in a low-rank subspace is ubiquitous throughout the signal estimation and detection literature and illuminates the important quantities impacting the KLD. From a physical perspective, a low-rank covariance indicates a significant degree of correlation among sensor readings, arising, e.g., when inter-element spacing is small.

Corollary 1. Assume the signal covariances Γ_0 and Γ_1 are low rank, such that $\Gamma_0 = (M/r)VV^H$ and $\Gamma_1 = (M/r)UU^H$, where $U, V \in \mathbb{C}^{M \times r}$ have orthonormal columns spanning the subspace corresponding to each set of parameters. Then

$$D(\theta_0||\theta_1) = M \text{SNR} \left(1 - \frac{1}{r} ||U^H V||_F^2 \frac{\text{SNR}}{\text{SNR} + r/M} \right)$$
$$- r \frac{\text{SNR}}{\text{SNR} + r/M}$$
(15)
$$= M \text{SNR} \left(\frac{\text{SNR}}{\text{SNR} + r/M} \left(1 - \frac{1}{r} ||U^H V||_F^2 \right) \right).$$
(16)

In this simplified setting, we see that the KLD is controlled by three terms: (1) the SNR, (2) the relative subspace dimension r/M, and (3) the squared subspace affinity $(1/r)\|U^HV\|_F^2$.

To examine the dependence on SNR, we first consider the setting where SNR $\geq r/M$ and the principal angles between subspaces are fixed. In this case, the term SNR/(SNR + r/M) is a constant less than 1, resulting in linear dependence on the SNR. In contrast, when SNR $\ll r/M$, the term SNR + $r/M \approx r/M$, making SNR/(SNR + r/M) $\approx M$ SNR/r. In this case, the KLD grows quadratically with SNR. Intuitively, this implies that in the low SNR regime, increasing the SNR results in a quadratic increase in KLD. However, once the SNR is sufficiently high (as determined by the rank of the signal covariance matrix), further increasing the SNR only provides a linear increase in KLD.

Next, we evaluate the dependence on the subspace dimension r. First note that the term $\|U^HV\|_F^2$ is the sum of r terms, and hence the 1/r is a normalizing constant that does not indicate the dependence of the KLD on the subspace

https://doi.org/10.1121/10.0022331

JASA

dimension. Hence, the impact of the subspace rank is primarily through the SNR/(SNR + r/M) term. In the case where $SNR \gg r/M$, the term $SNR/(SNR + r/M) \approx 1$; taking the view of Eq. (15), we see that the KLD decays linearly with r. However, when SNR is O(r) or smaller, the KLD decays as 1/r. In both settings, we see that the KLD decreases as r increases, i.e., low-dimensional signals are easier to distinguish than high-dimensional signals.

Finally, the term $(1/r)\|U^HV\|_F^2$ is the square of the *subspace affinity*³⁵ and is equivalent to $(1/r)\sum_{k=1}^r\cos^2(\eta_k)$, where η_k is the kth principal angle between the subspaces spanned by U and V.³⁶ The subspace affinity ranges from 0 to 1, with a value of 0 when the subspaces are orthogonal and a value of 1 when they are exactly the same. In this light, the term $1 - (1/r)\|U^HV\|_F^2$ is a function of the distance between subspaces, as measured by their principal angles. Equation (16) indicates that the KLD is monotone decreasing with the subspace affinity, having larger values for subspaces that are farther apart. Hence, we see that the difficulty in distinguishing between environmental parameters is impacted by both the rank of the underlying signal subspaces and how close the corresponding subspaces are to one another.

B. General setting

We now build on the above intuition to examine the general setting of Eq. (14). The key takeaway from this subsection is that nonuniformity in the eigenvalues helps distinguish between distributions, since the signal subspaces must be well aligned in terms of both directions (eigenvectors) and magnitude of energy in each direction (eigenvalues).

Note that the first term of Eq. (14) can be rewritten as

$$\operatorname{SNR}\left(M - \sum_{i=1}^{M} \sum_{j=1}^{M} \frac{\pi_{i} \lambda_{j} \operatorname{SNR}}{1 + \lambda_{j} \operatorname{SNR}} |u_{j}^{H} v_{i}|^{2}\right)$$

$$= \operatorname{SNR}\left(M - \|(UW)^{H} (V\Pi)\|_{F}^{2}\right), \tag{17}$$

where W is the diagonal matrix whose ith entry is $w_{ii} = \lambda_i \text{SNR}/(1 + \lambda_i \text{SNR})$. Under the general setting, we see that this term is large when the directions defined by u_j and v_i are well aligned and both covariances have large eigenvalues, corresponding to a large proportion of energy in these directions. In other words, although the signal subspaces may overlap significantly, the KLD may still be large if the energy in each distribution is concentrated in different directions.

Next consider the second term in Eq. (14)

$$\sum_{i=1}^{M} \frac{\lambda_i \text{SNR}}{1 + \lambda_i \text{SNR}},\tag{18}$$

where we recall that $\sum_{i=1}^{r} \lambda_i = M$. In the most extreme setting of non-equal eigenvalues, one direction dominates and Eq. (18) tends toward SNR/(1/M + SNR). This setting

corresponds to a signal covariance that is nearly unit rank, and hence nonuniformity has the impact of making the signal appear lower rank, which results in a larger KLD. In contrast, this term becomes r SNR/(r/M + SNR) in the low-rank, equal eigenvalue setting, which would result in a smaller KL divergence.

Finally, the third term in Eq. (14) is

$$\sum_{i=1}^{M} \log \left(\frac{\lambda_i \sigma_s^2 + \sigma_n^2}{\pi_i \sigma_s^2 + \sigma_n^2} \right). \tag{19}$$

For a fixed i, this term is zero if $\lambda_i = \pi_i$, positive if $\lambda_i > \pi_i$, and negative if $\pi_i < \lambda_i$. This term characterizes the difference in the distribution of eigenvalues for each set of parameters. For example, when two covariance matrices have the same eigenvectors (i.e., the same signal subspaces), this term captures the degree to which the energy is aligned in the same directions. In general, since the eigenvalues of both covariances sum to M, the summation consists of both positive and negative terms, and Eq. (19) is likely to have small impact relative to the first two terms.

IV. PERFORMANCE ANALYSIS

In this section, we evaluate the performance of hypothesis testing using the GLRT and relate these results to the KLD between the underlying distributions. We generate snapshots using MDANM,²² which can compute a covariance matrix from a set of environmental and ambient sound source parameters, as (1). MDANM is used here to compute K_{θ} matrices for a family of contrived scenarios in which only the properties of the seabed are varied. For surface-generated sound, MDANM employs a ray-theoretic model of the sound field to compute the directionality of the sound field.²³ This directionality is integrated against a directional sonar response model to produce a covariance matrix.

All simulations are for a shallow-water environment with a 32-element vertical line array having 0.15 m element spacing computed at 4.5 kHz. The only source is surface-generated sound and all environmental parameters for the surface, water, and bottom are homogeneous over range. The water depth is 100 m, and the water sound speed is approximately linearly downward refracting according to the top 100 m of a Munk profile.³⁷ The top of the receiver array is at 50 m. We note that the tools for hypothesis testing provided here depend only on the resulting covariance matrices, and hence one could directly apply the same approach to more complex, range-dependent environments, as well as a multi-layered seabed. Additionally, one could

TABLE I. Parameters and ranges used for evaluating hypothesis testing performance.

Parameter	Minimum	Maximum	Median
Sound speed (m / s)	1550	1650	1600.51
Bottom density (kg/m^3)	1030	2000	1519.90
Bottom attenuation (dB/λ)	0.01	0.2	0.11

https://doi.org/10.1121/10.0022331

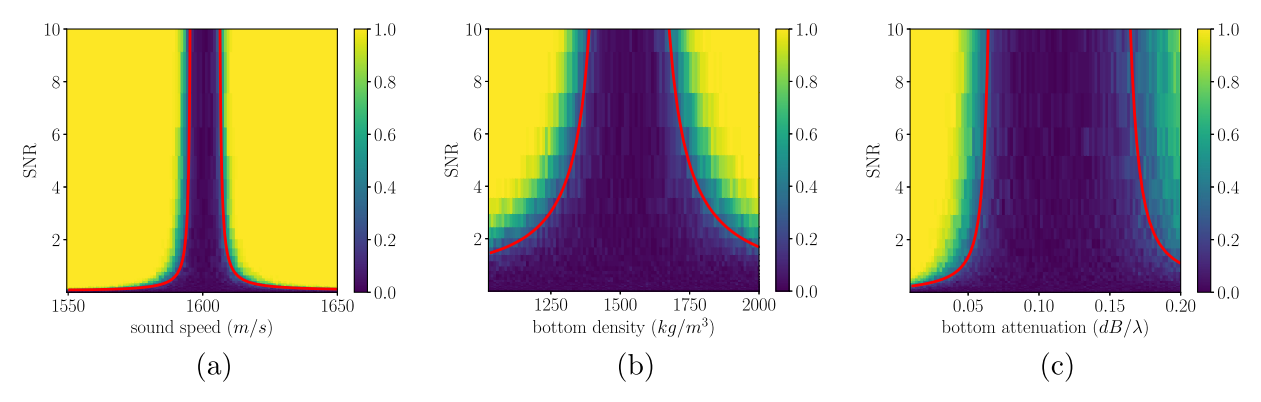


FIG. 2. (Color online) Relative frequency of selecting alternate hypothesis (seabed parameters are different) on data from MDANM as a function of SNR and (a) sound speed, (b) bottom density, and (c) bottom attenuation. The red lines indicate the theoretical limit as predicted by the KLD. For L snapshots, parameters resulting in a KLD less than $O(1/\sqrt{L})$ cannot be distinguished.

use this technique with a horizontal line array. However, a vertical aperture provides greater sensitivity to the vertical directivity of the ambient noise, and as such it contains a great deal of information about bottom reflectivity. Hence, we would expect that distinguishing between seabed types with a horizontal array would require a much higher SNR than doing so with a vertical array.

A. Limits of hypothesis testing

We first investigate the performance of the GLRT as we vary a single environmental parameter, considering a range of values for sound speed, bottom density, and bottom attenuation. The range of values for each parameter is given in Table I. We sweep each parameter over 100 values between the stated range, with the null hypothesis corresponding to the median value. We hold the other two parameters fixed at their median values. For each configuration, we draw L snapshots and perform hypothesis testing using the GLRT (8) with a level $\alpha = 0.01$. The results below display the mean over 100 Monte Carlo trials.

The relative frequency of selecting the alternate hypothesis as a function of seabed parameters and SNR is shown in Fig. 2, where L=300 snapshots are used for hypothesis testing. For each setting, we also calculate the KLD between the true distributions, displaying the $2/\sqrt{L}$ contour (red solid line), which corresponds to the absolute error in

parametric estimation of KLD. The figure shows a phase transition occurring at this contour, indicating that the KLD between seabed types must exceed this threshold in order to be distinguished, confirming our theoretical prediction in Sec. IIB. Further, we see that the ability to distinguish between two values of a given parameter increases rapidly in the low-SNR regime, corresponding to the prediction that for low SNR, the KLD increases quadratically. In contrast, for sufficiently high SNR [e.g., SNR \geq 3 in Fig. 2(c)], the ability to resolve a given parameter only improves linearly with SNR.

To further verify the dependence on the number of snapshots, we fix the SNR to 5 and evaluate performance as the number of snapshots ranges from 100–1000. The relative frequency of selecting the alternate hypothesis as a function of seabed parameters and the number of snapshots is displayed in Fig. 3. As in the previous case, we see a phase transition at the predicted bound, indicating that Eq. (13) can be used to quantify when hypothesis testing can successfully distinguish between environmental parameters.

We next to turn to Theorem 1 as a means of explaining why hypothesis testing fails for a given setting. From Fig. 2, we see that sound speed is significantly easier to distinguish than bottom attenuation and that distinguishing bottom attenuation to the right of the median is more difficult than to the left. To understand why this behavior appears, we first evaluate the intrinsic rank of the signal subspace as a function of each seabed parameter, recalling that the KL

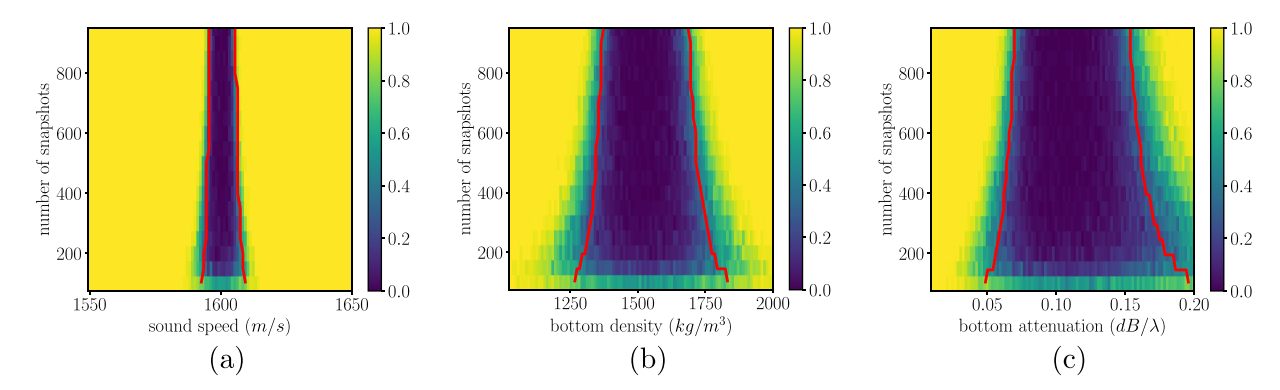


FIG. 3. (Color online) Relative frequency of selecting alternate hypothesis (seabed parameters are different) on data from MDANM as a function of number of snapshots *L* and (a) sound speed, (b) bottom density, and (c) bottom attenuation. The red lines indicate the theoretical limit as predicted by the KLD.

https://doi.org/10.1121/10.0022331



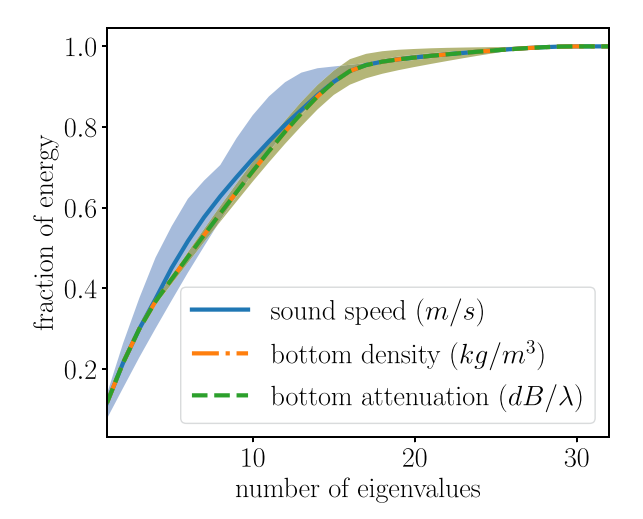


FIG. 4. (Color online) Fraction of energy in first *r* eigenvalues as measured by Eq. (20). The figure indicates that the covariance is approximately low rank, regardless of parameter considered.

divergence becomes smaller as the rank increases. Define the fraction of energy in the first r eigenvalues as

$$\frac{\sum_{i=1}^{r} \lambda_i}{\sum_{i=1}^{M} \lambda_i}.$$
 (20)

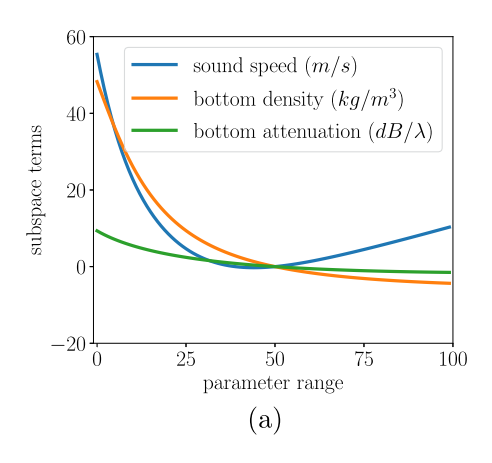
This fraction is shown in Fig. 4 as each parameter varies across its range. For each parameter, we compute Eq. (20) for all 100 values and display the median along with the maximum and minimum. For a matrix that is nearly low rank, this fraction is expected to increase rapidly until the intrinsic dimension is reached, often accounting for 90% or more of the energy in a small number of singular values. The figure shows that the median value of Eq. (20) surpasses 0.9 for a rank of r = 15 across all seabed parameters, indicating that the increased difficulty of distinguishing between different values of bottom attenuation is not due to a difference in rank.

Having established that all signal subspaces have approximately the same rank, we next examine the relationship between the subspaces themselves, as well as the distribution of eigenvalues, as a function of each parameter. To do this, we break the KLD into the *subspace terms*, corresponding to the

first two terms in Eq. (14), and the eigenvalue term, which corresponds to the third term in the equation. The subspace and eigenvalue terms are displayed separately in Fig. 5, where we vary each parameter over the corresponding range of values. To better evaluate the impact of the underlying signal covariance matrices, we set the SNR to 100 000 removing its impact on KLD. The figure illuminates the differences in difficulty as each parameter varies. Namely, we see that the signal subspaces for varying sound speed have large variation, while the distribution of eigenvalues is similar across all values, keeping the eigenvalue term relatively small. In contrast, varying bottom attenuation has little impact on the signal subspace. Further, the signal subspaces are nearly equal as bottom attenuation takes values greater than the midpoint, accounting for the asymmetry in hypothesis testing shown in Fig. 2(c). For bottom density, we observe strong subspace variation for values below the midpoint. As the parameter proceeds beyond the midpoint, the signal subspace shows little variation, but the difference in the distribution of eigenvalues is sufficient to provide differentiation between the corresponding distributions. Exploiting this difference in eigenvalue distributions may provide a means of obtaining finer resolution for both bottom density and bottom attenuation and is a topic for our future research.

B. Bottom sediment type database

Finally, we evaluate the KLD between the sediment types defined in the HFEVA dataset, in order to gain an understanding of which types can be distinguished using ambient sound. The HFEVA dataset details 23 sediment categories including various types and combinations of rock, sand, silt, and clay. In general, the seabed reflectivity decreases with HFEVA's sediment type index, with highly reflective types corresponding to lower indices. To keep the number of parameters to a minimum, all boundary interactions handled as Rayleigh reflection coefficients, which depend only on density, sound speed, and attenuation. HFEVA also contains parameters that affect scattering, but these are ignored since scattering is not enabled in the simulation. We utilize MDANM to generate covariance matrices and bottom loss curves for categories 2–23, since categories 1 and 2 (rough rock and rock) are the same in all parameters except scattering. The seabed types and corresponding parameters are given in Table II, Appendix C, where the



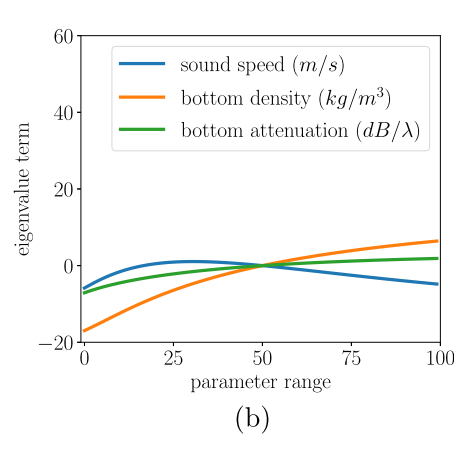


FIG. 5. (Color online) KLD separated into terms describing the signal subspaces (subspace terms) and the distribution of eigenvalues (eigenvalue term) as a function of seabed parameters. (a) Subspace terms refer to the first two terms of Eq. (14). (b) Eigenvalue term is the final term of Eq. (14).

27 August 2024 17:36:49

https://doi.org/10.1121/10.0022331

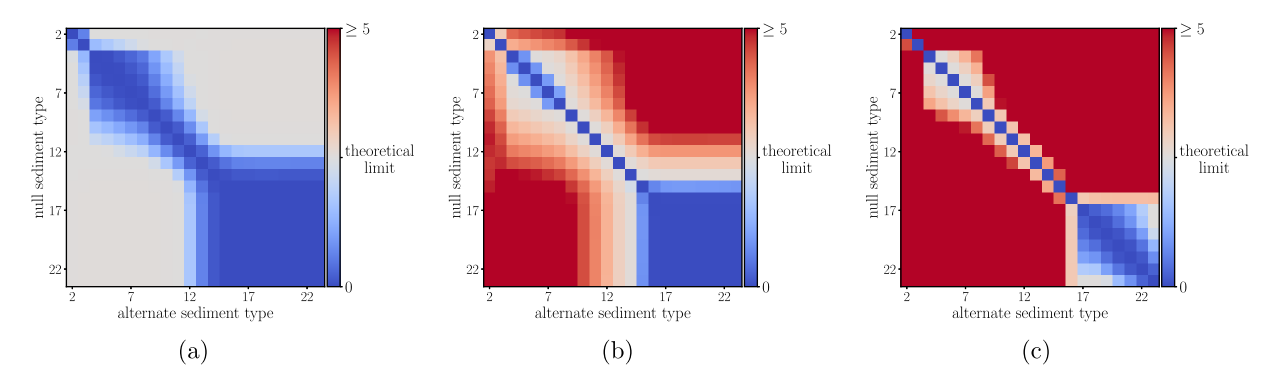


FIG. 6. (Color online) KLD of alternate sediment type (horizontal axis) from null sediment type (vertical axis) for 22 sediment types defined in the HFEVA database. The theoretical limit is set to $2/\sqrt{(L)}$ with L=300 snapshots. Blue values indicate the pairs of sediment types cannot be reliably distinguished. (a) SNR=0.1. (b) SNR=1. (c) SNR=100000.

parameter values are taken from the High-Frequency Ocean Environmental Acoustic Models Handbook.[?]

The KLD between sediment types for varying SNR is displayed in Fig. 6, with the theoretical limit based on obtaining L = 300 snapshots. The heatmap is scaled so that shades of red are distinguishable from L snapshots, shades of blue are indistinguishable, and gray indicates the KLD is near the theoretical limit. As expected, sequential categories are the most difficult to distinguish, since these share the most similar sound speed and densities. Although obscured by the color scaling, a greater difference in seabed type generally corresponds to a greater KLD, though for some types this relationship does not hold. Next, we see that for an SNR of 0.1, no categories are above the theoretical limit by a substantial amount, while at an SNR of 1, many categories can be distinguished. Finally, we see that even in the unrealistic setting of SNR = 100000 many sequential categories are still indistinguishable. In particular, distinguishing categories 17–23, which correspond to various combinations of fine silt and clay, is essentially impossible from an information-theoretic perspective.

We display the KLD for a fixed SNR = 10 in Fig. 7, varying the theoretical limit to correspond to $L=100,\,1000,\,1000,\,1000,\,10000$ snapshots. As expected, increasing the number of snapshots results in additional resolution among sediment types. However, even in the limit of $L=100\,000,\,10000,\,10000$ categories 17–23 remain indistinguishable for the particular array configuration considered here.

To confirm the above findings, we examine the bottom loss as a function of grazing angle for a few sediment types of interest. The bottom loss curves for sediment types (a) 2-5, (b) 15–19, and (c) 19–23 are displayed in Fig. 8. In all cases, the visual similarities between bottom loss curves follow those indicated by KLD. For example, Fig. 6 indicates that types 2 and 3 (rock and cobble) are easily distinguishable, whereas types 4 and 5 (sandy gravel and very coarse sand) have a KLD that is always below or very close to the theoretical limit, indicating they are essentially indistinguishable. Similarly, sediment type 15 (coarse silt) is easily distinguishable from types 17–19, corresponding to its red KLD in Figs. 6 and 7. However, types 17–23 show minimal variation in bottom loss, with 19-23 showing almost no difference. This is confirmed in Fig. 7, which shows that for a very large number of snapshots, 17 and 18 may be distinguishable from 19-23, whereas 19-23 remain indistinguishable. Although not pictured, similar conclusions can be drawn by comparing the KLD and bottom loss curves for types 6–14. Hence, we see that the KLD provides an alternative, quantitative perspective on when seabed types can be distinguished that conforms to the traditional approach of examining bottom loss. Finally, we note that one could classify sediment type by choosing the type of smallest KLD. However, such a classifier relies on the assumption that the number of layers and parameters in the seabed model are correct and therefore requires additional knowledge of the environment. Alternatively, once the snapshots are sorted via hypothesis testing, any form of geoacoustic

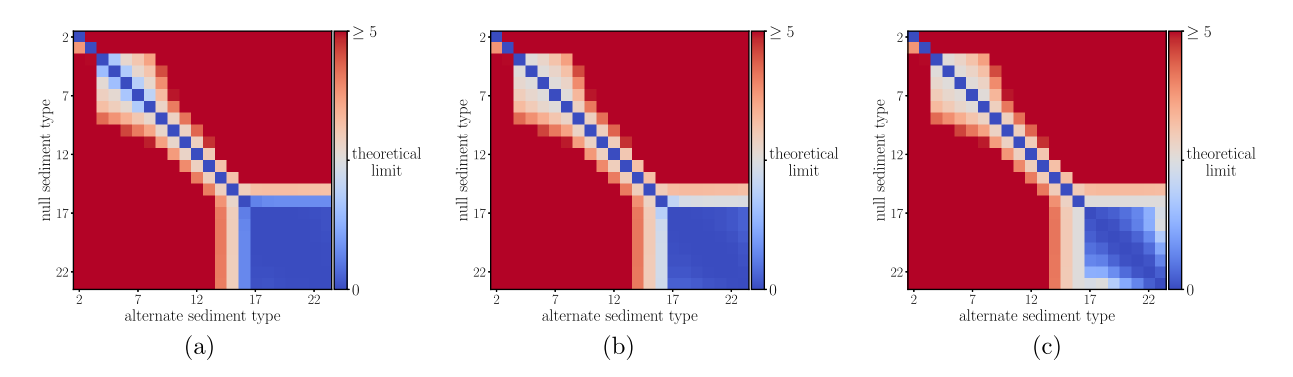


FIG. 7. (Color online) KLD of alternate sediment type (horizontal axis) from null sediment type (vertical axis) for 22 sediment types defined in the HFEVA database for varying number of snapshots L. The theoretical limit is set to $2/\sqrt{(L)}$ and SNR = 10. Blue values indicate the pairs of sediment types cannot be reliably distinguished. (a) L = 100. (b) L = 1000. (c) L = 100000.

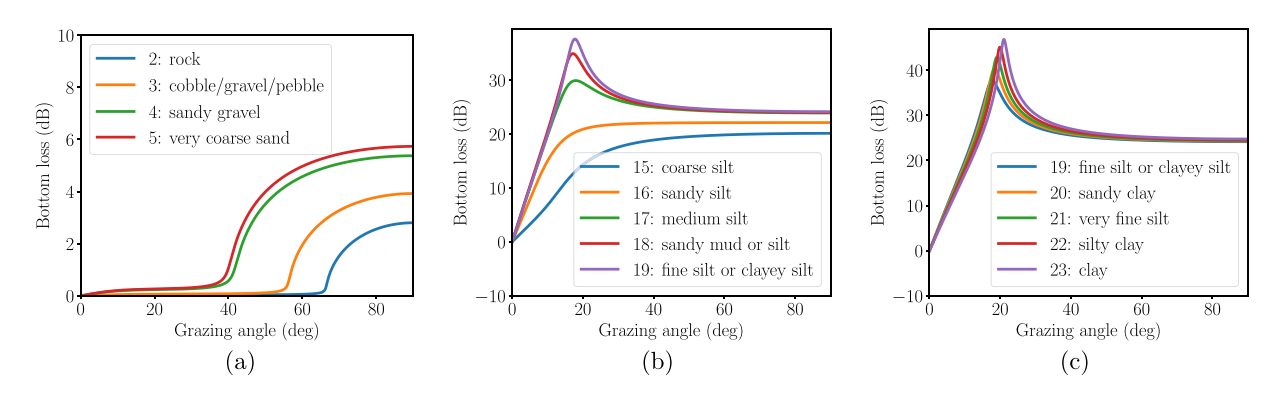


FIG. 8. (Color online) Bottom loss plots for sediment types (a) 2–5 ("rock"-"very coarse gravel"), (b) 15-19 ("coarse silt"-"fine silt"), and (c) 19-23 ("fine silt"-"clay"). The similarity of bottom loss curves corresponds to the KLD indicated by Figs. 6 and 7.

inversion could be used to more accurately estimate the true seabed model and parameters.

V. CONCLUSION

This article presents an approach to distinguishing between seabed parameters or sediment types using wind-driven ambient sound as a source for a passive sonar array. The framework of hypothesis testing provides an optimal means of testing whether collections of snapshots from two distinct locations share environmental parameters, and the test for the case of circularly symmetric Gaussian snapshots is a function of the KLD between the underlying distributions. Hence, a deeper analysis of the KLD for this setting provides theoretical insights into when seabed parameters can be distinguished and why. In particular, our analysis frames these questions in terms of the underlying signal subspaces corresponding to differing environmental models, as well as the SNR.

Empirical observations on acoustic snapshots simulated by MDANM demonstrate that the success of hypothesis testing matches the theoretical limit predicted by the KLD. It is impossible for the given array to distinguish between environmental parameters whose corresponding KLD is below the estimation error incurred by performing hypothesis testing from a finite number of snapshots. When considering sediment types defined by the HFEVA dataset, we see that numerous types are indistinguishable, even for a very large SNR or number of snapshots. This observation could be used to drive array design, allowing the user to guarantee that sediment types of interest would be distinguishable at a reasonable SNR.

The analysis technique presented here could be used to evaluate the impact of less well-behaved sound sources, such as ship traffic or biologic activity. An additional avenue for future work could be that of evaluating the impact of parameter misclassification on sonar performance. While certain sediment types are indistinguishable in our setting, it may be the case that these types are similar enough to have little impact on sonar performance.

ACKNOWLEDGMENTS

J.L. was supported by Defense Advanced Research Projects Agency YFA Award No. D22AP00135 and National Science Foundation Award No. CAREER CIF- 2046175. M.S. was supported by Office of Naval Research Ocean Acoustics Program Grant No. N00014-23-1-2070.

AUTHOR DECLARATIONS Conflict of Interest

The authors have no conflicts of interest to disclose.

DATA AVAILABILITY

The data that support the findings of this study are available from the corresponding author upon reasonable request.

APPENDIX A: DERIVATION OF GLRT STATISTIC

Beginning from the definition of the joint PDF of circularly symmetric Gaussian random vectors, we obtain the test statistic below,

$$\Lambda(x_{1},...,x_{L}) = 2 \log \left[\frac{\prod_{i=1}^{L} \det(\pi \hat{K})^{-1} \exp\left(-x_{i}^{H} \hat{K}^{-1} x_{i}\right)}{\prod_{i=1}^{L} \det(\pi K_{0})^{-1} \exp\left(-x_{i}^{H} K_{0}^{-1} x_{i}\right)} \right]$$

$$= 2 \log \left[\frac{\det(\pi \hat{K})^{-L}}{\det(\pi K_{0})^{-L}} \times \exp\left(-\sum_{i=1}^{L} x_{i}^{H} \left(\hat{K}^{-1} - K_{0}^{-1}\right) x_{i}\right) \right]$$

$$= 2L \log \frac{\det(K_{0})}{\det(\hat{K})} - 2 \sum_{i=1}^{L} x_{i}^{H} \left(\hat{K}^{-1} - K_{0}^{-1}\right) x_{i}$$

$$= 2L \log \frac{\det(K_{0})}{\det(\hat{K})}$$

$$- 2 \operatorname{tr} \left(\sum_{i=1}^{L} x_{i} x_{i}^{H} \left(\hat{K}^{-1} - K_{0}^{-1}\right)\right)$$

$$= 2L \log \frac{\det(K_{0})}{\det(\hat{K})} - 2 \operatorname{tr} \left(L \hat{K} \left(\hat{K}^{-1} - K_{0}^{-1}\right)\right)$$

$$= 2L \log \frac{\det(K_{0})}{\det(\hat{K})} - 2 \operatorname{tr}(LI) + 2 \operatorname{tr} \left(L \hat{K} K_{0}^{-1}\right)$$

$$= 2L \left(\log \frac{\det(K_{0})}{\det(\hat{K})} - M + \operatorname{tr} \left(K_{0}^{-1} \hat{K}\right)\right).$$

APPENDIX B: PROOF OF THEOREM 1

The proof relies on the matrix inversion lemma and the matrix determinant lemma. Applying the eigenvalue decomposition to Γ_1 , we write

$$K_1 = \sigma_r^2 I + U \sigma_s^2 \Lambda U^H$$

Applying the matrix inversion lemma yields

$$K_{1}^{-1} = \frac{1}{\sigma_{n}^{2}} I - \frac{1}{\sigma_{n}^{2}} U \left(\frac{1}{\sigma_{s}^{2}} \Lambda^{-1} + U^{H} \frac{1}{\sigma_{n}^{2}} IU \right)^{-1} U^{H} \frac{1}{\sigma_{n}^{2}}$$
$$= \frac{1}{\sigma_{n}^{2}} (I - UDU^{H}),$$

where we define the diagonal matrix $D \in \mathbb{R}^{M \times M}$ to have diagonal elements of the form

$$d_{ii} = \frac{\lambda_i \sigma_s^2}{\lambda_i \sigma_s^2 + \sigma_n^2}.$$

Writing $\Gamma_0 = V \Pi V^H$ yields

$$K_1^{-1}K_0 = I + \frac{\sigma_s^2}{\sigma_n^2}V\Pi V^H - UDU^H - \frac{\sigma_s^2}{\sigma_n^2}UDU^HV\Pi V^H.$$

Since the trace is a linear operation, we examine the trace of each term individually. The first term yields tr(I) = M. For the second term, we apply the cyclic permutation property to see that

$$\operatorname{tr}\left(\frac{\sigma_{s}^{2}}{\sigma_{n}^{2}}V\Pi V^{H}\right) = M\frac{\sigma_{s}^{2}}{\sigma_{n}^{2}}\operatorname{tr}(V^{H}V\Pi)$$
$$= \frac{\sigma_{s}^{2}}{\sigma_{n}^{2}}\operatorname{tr}(\Pi)$$
$$= \frac{\sigma_{s}^{2}}{\sigma_{n}^{2}} = M \cdot \operatorname{SNR},$$

where we use the assumption that the eigenvalues of Γ_0 sum to M. Similarly, we see that

$$\operatorname{tr}(UDU^{H}) = \sum_{i=1}^{M} \frac{\lambda_{i}\sigma_{s}^{2}}{\lambda_{i}\sigma_{s}^{2} + \sigma_{n}^{2}}.$$

Finally, note that $tr(UDU^HV\Pi V^H) = tr(V^HUDU^HV\Pi)$. Further inspection of the matrix $V^HUDU^HV\Pi$ shows that its diagonal elements are of the form

$$[V^H U D U^H V \Pi]_{ii} = \pi_i \sum_{i=1}^M d_{jj} |u_j^H v_i|^2.$$

Taking the trace of this term yields

$$\operatorname{tr}(UDU^{H}V\Pi V^{H}) = \sum_{i=1}^{M} \pi_{i} \sum_{j=1}^{M} d_{jj} |u_{j}^{H} v_{i}|^{2}$$

$$= \sum_{i=1}^{M} \sum_{j=1}^{M} \frac{\pi_{i} \lambda_{j} \sigma_{s}^{2}}{\lambda_{j} \sigma_{s}^{2} + \sigma_{n}^{2}} |u_{j}^{H} v_{i}|^{2}$$

$$= \sum_{i=1}^{M} \sum_{j=1}^{M} \frac{\pi_{i} \lambda_{j} \operatorname{SNR}}{\lambda_{j} \operatorname{SNR} + 1} |u_{j}^{H} v_{i}|^{2}.$$

Combining all terms under the trace, we see that

$$\operatorname{tr}(K_1^{-1}K_0) = M + M\operatorname{SNR} - \sum_{i=1}^{M} \frac{\lambda_i \operatorname{SNR}}{\lambda_i \operatorname{SNR} + 1} + \sum_{i=1}^{M} \sum_{j=1}^{M} \frac{\pi_i \lambda_j \operatorname{SNR}}{\lambda_j \operatorname{SNR} + 1} |u_j^H v_i|^2.$$

Next, we evaluate the third term in Eq. (10). To evaluate $\det(K_1)$, we define the $2M \times 2M$ real-valued matrix

$$ar{K}_1 = \sigma_s^2 \left[egin{array}{ll} \Gamma_1^{(\mathrm{re})} & -\Gamma_1^{(\mathrm{im})} \ \Gamma_1^{(\mathrm{im})} & \Gamma_1^{(\mathrm{re})}. \end{array}
ight] + \sigma_n^2 I_{2M} =: \sigma_s^2 ar{\Gamma}_1 + \sigma_n^2 I_{2M},$$

where I_{2M} denotes the identity of size $2M \times 2M$. Next, note $\bar{\Gamma}$ has M unique eigenvalues, each repeated twice, and that these are exactly the M eigenvalues of Γ . Finally, note that

$$\det(\bar{K}_1) = |\det(K_1)|^2.$$

Letting $\bar{\Gamma}_1 = \bar{U}\bar{\Lambda}\bar{U}^T$, we apply the matrix determinant lemma to see that

$$\begin{split} \det(\bar{K}_1) &= \det\left(\sigma_n^2 I_{2M} + \sigma_s^2 \bar{U} \bar{\Lambda} \bar{U}^T\right) \\ &= \det\left(\frac{1}{\sigma_s^2} \bar{\Lambda}^{-1} + \frac{1}{\sigma_n^2} \bar{U}^T \bar{U}\right) \det\left(\sigma_s^2 \bar{\Lambda}\right) \det\left(\sigma_n^2 I_{2M}\right) \\ &= \left(\sigma_s^2 \sigma_n^2\right)^{2M} \det\left(\frac{1}{\sigma_s^2} \bar{\Lambda}^{-1} + \frac{1}{\sigma_n^2} I_{2M}\right) \det(\bar{\Lambda}) \\ &= \left(\sigma_s^2 \sigma_n^2\right)^{2M} \prod_{i=1}^{2M} \frac{\bar{\lambda}_i \sigma_s^2 + \sigma_n^2}{\sigma_s^2 \sigma_n^2} \\ &= \left(\left(\sigma_s^2 \sigma_n^2\right)^M \prod_{i=1}^{M} \frac{\lambda_i \sigma_s^2 + \sigma_n^2}{\sigma_s^2 \sigma_n^2}\right)^2, \end{split}$$

where we recall that λ_i is the *i*th eigenvalue of the matrix Γ_1 . The above implies that

$$\det(K_1) = \left(\sigma_s^2 \sigma_n^2\right)^M \prod_{i=1}^M \frac{\lambda_i \sigma_s^2 + \sigma_n^2}{\sigma_s^2 \sigma_n^2},$$

where we may consider only the solution to $\sqrt{\det(\bar{K}_1)}$, since any positive semidefinite matrix must have a nonnegative determinant. Similarly,

$$\det(K_0) = \left(\sigma_s^2 \sigma_n^2\right)^M \prod_{i=1}^M \frac{\pi_i \sigma_s^2 + \sigma_n^2}{\sigma_s^2 \sigma_n^2}.$$

Plugging the above terms into Eq. (10) completes the proof.

APPENDIX C: ENVIRONMENTAL PARAMETERS FOR HFEVA SEDIMENT TYPES

Note that all parameters are ratios and therefore unitless. The density ratio is the ratio of sediment mass density to water mass density, the sound speed ratio is the ratio of

27 August 2024 17:36:49



TABLE II. Seabed types and parameter values for HFEVA dataset.

Category	Name	Density Ratio	Sound Speed Ratio	Loss
1	Rough Rock	2.5	2.5	1.374×10^{-2}
2	Rock	2.5	2.5	1.374×10^{-2}
3	Cobble/Gravel/Pebble	2.5	1.8	1.375×10^{-2}
4	Sandy Gravel	2.492	1.3376	1.705×10^{-2}
5	Very Coarse Gravel	2.401	1.3067	1.667×10^{-2}
6	Muddy Sandy Gravel	2.314	1.2778	1.630×10^{-2}
7	Coarse Sand/Gravelly Sand	2.231	1.2503	1.638×10^{-2}
8	Gravelly Muddy Sand	2.151	1.2241	1.645×10^{-2}
9	Medium Sand/Sand	1.845	1.1782	1.624×10^{-2}
10	Muddy Gravel	1.615	1.1396	1.610×10^{-2}
11	Fine Sand/Silty Sand	1.451	1.1073	1.602×10^{-2}
12	Muddy Sand	1.339	1.0806	1.725×10^{-2}
13	Very Fine Sand	1.268	1.0568	1.875×10^{-2}
14	Clayey Sand	1.224	1.0364	2.019×10^{-2}
15	Coarse Silt	1.195	1.0179	2.158×10^{-2}
16	Gravelly Mud/Sandy Silt	1.169	0.9999	1.261×10^{-2}
17	Medium Silt / Sand-Silt-Clay	1.149	0.9885	0.676×10^{-2}
18	Sandy Mud/Silt	1.149	0.9873	0.386×10^{-2}
19	Fine Silt/Clayey Silt	1.148	0.9861	0.306×10^{-2}
20	Sandy Clay	1.147	0.9849	0.242×10^{-2}
21	Very Fine Silt	1.147	0.9837	0.194×10^{-2}
22	Silty Clay	1.146	0.9824	0.163×10^{-2}
23	Clay	1.145	0.9806	0.148×10^{-2}

sediment sound speed to water sound speed, and the loss parameter is the ratio of imaginary wavenumber to real wavenumber for the sediment.³⁸

¹E. L. Hamilton, "Geoacoustic models of the sea floor," in *Physics of Sound in Marine Sediments* (Springer, Berlin, 1974), pp. 181–221.

²D. R. Del Balzo, J. H. Leclere, and M. J. Collins, "Critical angle and seabed scattering issues for active-sonar performance predictions in shallow water," in *High Frequency Acoustics in Shallow Water*, Lerici, Italy (NATOSACLANT Undersea Research Centre, La Spezia, Italy, 1997).

³M. Prior, C. Harrison, and S. Healy, "Assessment of the impact of uncertainty in seabed geoacoustic parameters on predicted sonar performance," in *Impact of Littoral Environmental Variability of Acoustic Predictions and Sonar Performance* (Springer, Berlin, 2002), pp. 531–538.

⁴C. Park, W. Seong, and P. Gerstoft, "Geoacoustic inversion in time domain using ship of opportunity noise recorded on a horizontal towed array," J. Acoust. Soc. Am. **117**(4), 1933–1941 (2005).

⁵L. Muzi, M. Siderius, and C. M. Verlinden, "Passive bottom reflection-loss estimation using ship noise and a vertical line array," J. Acoust. Soc. Am. **141**(6), 4372–4379 (2017).

⁶E. L. Ferguson, R. Ramakrishnan, S. B. Williams, and C. T. Jin, "Convolutional neural networks for passive monitoring of a shallow water environment using a single sensor," in 2017 IEEE International Conference on Acoustics, Speech and Signal Processing (ICASSP) (IEEE, Piscataway, NJ, 2017), pp. 2657–2661.

⁷M. Siderius and J. Gebbie, "Environmental information content of ocean ambient noise," J. Acoust. Soc. Am. **146**(3), 1824–1833 (2019).

⁸J. Gebbie and M. Siderius, "Optimal environmental estimation with ocean ambient noise," J. Acoust. Soc. Am. **149**(2), 825–834 (2021).

⁹D. P. Knobles, P. S. Wilson, J. A. Goff, L. Wan, M. J. Buckingham, J. D. Chaytor, and M. Badiey, "Maximum entropy derived statistics of sound-speed structure in a fine-grained sediment inferred from sparse broadband acoustic measurements on the New England continental shelf," IEEE J. Oceanic Eng. 45(1), 161–173 (2020).

¹⁰M. Siderius, C. H. Harrison, and M. B. Porter, "A passive fathometer technique for imaging seabed layering using ambient noise," J. Acoust. Soc. Am. 120, 1315–1323 (2006). ¹¹J. Li, P. Gerstoft, M. Siderius, and J. Fan, "Inversion of head waves in ocean acoustic ambient noise," J. Acoust. Soc. Am. 147(3), 1752–1761 (2020).

¹²C. H. Harrison and D. G. Simons, "Geoacoustic inversion of ambient noise: A simple method," J. Acoust. Soc. Am. 112, 1377–1389 (2002).

¹³K. D. Heaney, "Rapid geoacoustic characterization using a surface ship of opportunity," IEEE J. Oceanic Eng. 29(1), 88–99 (2004).

¹⁴K. D. Heaney, G. Gawarkiewicz, T. F. Duda, and P. F. Lermusiaux, "Nonlinear optimization of autonomous undersea vehicle sampling strategies for oceanographic data-assimilation," J. Field Rob. 24(6), 437–448 (2007).

¹⁵M. J. Bianco, P. Gerstoft, J. Traer, E. Ozanich, M. A. Roch, S. Gannot, and C.-A. Deledalle, "Machine learning in acoustics: Theory and applications," J. Acoust. Soc. Am. 146(5), 3590–3628 (2019).

¹⁶J. Piccolo, G. Haramuniz, and Z.-H. Michalopoulou, "Geoacoustic inversion with generalized additive models," J. Acoust. Soc. Am. **145**(6), EL463–EL468 (2019).

¹⁷D. Van Komen, T. B. Neilsen, D. P. Knobles, and M. Badiey, "A convolutional neural network for source range and ocean seabed classification using pressure time-series," Proc. Mtgs. Acoust. 36, 070004 (2019).

¹⁸C. Frederick, S. Villar, and Z.-H. Michalopoulou, "Seabed classification using physics-based modeling and machine learning," J. Acoust. Soc. Am. 148(2), 859–872 (2020).

¹⁹D. F. Van Komen, T. B. Neilsen, K. Howarth, D. P. Knobles, and P. H. Dahl, "Seabed and range estimation of impulsive time series using a convolutional neural network," J. Acoust. Soc. Am. 147(5), EL403–EL408 (2020)

²⁰K. Howarth, T. B. Neilsen, D. F. Van Komen, and D. P. Knobles, "Seabed classification using a convolutional neural network on explosive sounds," IEEE J. Oceanic Eng. 47, 670–679 (2022).

²¹Naval Oceanographic Office Acoustics Division, "Database description for bottom sediment type (U)" (2003).

²²Naval Oceanographic Office Acoustics Division, "Software design description and software test description for the multi-dimensional ambient noise model (MDANM) version 1.01 (U)" (2022).

²³C. Harrison, "Formulas for ambient noise level and coherence," J. Acoust. Soc. Am. **99**(4), 2055–2066 (1996).

²⁴W. A. Kuperman and F. Ingenito, "Spatial correlation of surface generated noise in a stratified ocean," J. Acoust. Soc. Am. 67(6), 1988–1996 (1980).

²⁵L. Wasserman, All of Statistics: A Concise Course in Statistical Inference (Springer, Berlin, 2004), Vol. 26.

JASA

https://doi.org/10.1121/10.0022331

- ²⁶S. M. Kay, Fundamentals of Statistical Signal Processing: Estimation Theory (Prentice-Hall, Hoboken, 1993).
- ²⁷S. Kullback and R. A. Leibler, "On information and sufficiency," Ann. Math. Stat. 22(1), 79–86 (1951).
- ²⁸M. I. Taroudakis, G. Tzagkarakis, and P. Tsakalides, "Classification of shallow-water acoustic signals via alpha-stable modeling of the onedimensional wavelet coefficients," J. Acoust. Soc. Am. 119(3), 1396–1405 (2006).
- ²⁹C. Smaragdakis and M. I. Taroudakis, "Acoustic signal characterization based on hidden Markov models with applications to geoacoustic inversions," J. Acoust. Soc. Am. 148(4), 2337–2350 (2020).
- ³⁰Y. Park, F. Meyer, and P. Gerstoft, "Graph-based sequential beamforming," J. Acoust. Soc. Am. 153(1), 723–737 (2023).
- ³¹P. Moulin and V. V. Veeravalli, Statistical Inference for Engineers and Data Scientists (Cambridge University Press, Cambridge, 2018).

- ³²Z. Harchaoui, F. Bach, O. Cappe, and E. Moulines, "Kernel-based methods for hypothesis testing: A unified view," IEEE Signal Process. Mag. 30(4), 87–97 (2013).
- ³³T. M. Cover, *Elements of Information Theory* (Wiley, New York, 1999).
- ³⁴R. Vershynin, High-Dimensional Probability: An Introduction with Applications in Data Science (Cambridge University Press, Cambridge, 2018), Vol. 47.
- ³⁵M. Soltanolkotabi and E. J. Candés, "A geometric analysis of subspace clustering with outliers," Ann. Stat. 40, 2195–2238 (2012).
- ³⁶G. H. Golub and C. F. Van Loan, *Matrix Computations* (John Hopkins University Press, Baltimore, MD, 2013).
- ³⁷W. H. Munk, "Sound channel in an exponentially stratified ocean, with application to SOFAR," J. Acoust. Soc. Am. 55(2), 220–226 (1974).
- ³⁸A. H. Sayed, *Adaptive Filters* (John Wiley & Sons, New York, 2011).